Remote Sensing of Environment 265 (2021) 112664

Contents lists available at ScienceDirect

Remote Sensing of Environment

journal homepage: www.elsevier.com/locate/rse

Hydrological control shift from river level to rainfall in the reactivated Guobu slope besides the Laxiwa hydropower station in China

Xuguo Shi [a], Xie Hu [b,*], Nicholas Sitar [c], Robert Kayen [c], Shengwen Qi [d], Houjun Jiang [e], Xudong Wang [a], Lu Zhang [f]

[a] School of Geography and Information Engineering, China University of Geosciences, Wuhan, China
[b] College of Urban and Environmental Sciences, Peking University, Beijing, China
[c] Department of Civil and Environmental Engineering, University of California, Berkeley, CA, USA
[d] Key Laboratory of Shale Gas and Geoengineering, Institute of Geology and Geophysics, Chinese Academy of Sciences, Beijing, China
[e] School of Civil Engineering, Anhui Jianzhu University, Hefei, Anhui, China
[f] State Key Laboratory of Information Engineering in Surveying, Mapping and Remote Sensing, Wuhan University, Wuhan, China

ARTICLE INFO

Edited by Jing M. Chen

Keywords:
Triggered landslide
Hydroclimatic controls
InSAR
Hydraulic diffusivity
The Guobu slope

ABSTRACT

Landslides are common geohazards associated with natural drivers such as precipitation, land degradation, toe erosion by rivers and wave attack, and ground shaking. On the other hand, human alterations such as inundation by water impoundment or rapid drawdown may also destabilize the surrounding slopes. The Guobu slope is an ancient rockslide on the banks of the Laxiwa hydropower station reservoir (China), which reactivated during the reservoir impoundment in 2009. We extracted three-dimensional surface displacements with azimuth and range radar interferometry using European Space Agency's Copernicus Sentinel-1 and German Aerospace Center's TerraSAR-X data during 20152019. The upper part of the Guobu rockslide is characterized by toppling and is mostly subsiding with maximum rates over 0.4 m/yr and 0.7 m/yr in the vertical and horizontal directions, respectively. During filling of the reservoir prior to 2014, there was a long-wavelength in-phase response between rising reservoir level and GPS-observed increased slope movements. After the reservoir water level stabilized from 2015 to 2019, the slide movement became seasonal and we see a correlation between rainfall and landslide movement. These observations suggest that the slide motion is now primarily controlled by rainfall. The spatiotemporal landslide displacements allow us to estimate the hydraulic diffusivity of the rock mass, to be on the order ($\sim 1.05 \times 10^{-7}$ m^2/s) and the thickness of the moving rock mass (~200 m). Our results demonstrate that InSAR is a useful tool for monitoring the rockslide movement as a function of seasonal precipitation.

1. Introduction

It is well recognized that rapid impoundment and cyclic filling and lowering reservoir levels can perturb the bank slope stability (Chen et al., 2017; Paronuzzi et al., 2013; Qi et al., 2017). For example, more than 500 landslides occurred between 1941 and 1953 in the Roosevelt Lake formed by the Grand Coulee Dam construction (USA), causing a great economic loss (Schuster, 1979). Over 600 out more than 2,600 preexisting landslides reactivated along the banks of the reservoir of the Three Gorges Dam (China) since it started filling in 2003, and 8 failed completely (Tang et al., 2019). Among them the 2003 Qianjiangping slope failure occurred shortly after an abrupt rise in water level of Qinggan River, a tributary of the Yangtze River, from 70 m to 135 m, causing more than 14 casualties (Wang et al., 2008). The 1963 Vajont landslide (Italy) was observed moving at a maximum rate of 80 mm/day after the first impoundment of the Vajont Dam in November 1960 (Müller-Salzburg, 1987). The eventual catastrophic failure created a reservoir surge that destroyed several villages and claimed more than two thousand lives. On a global scale, many unstable slopes may be found around more than 38,000 dams and the corresponding reservoir areas (Mulligan et al., 2020). Therefore, detecting and monitoring active slopes and evaluating the magnitude of the slope movements are critical for hazard mitigation and risk assessment in reservoir impoundment. Conventional slope monitoring methods can only obtain sparse measurements at a few locations on or within the affected slopes, such as from Global Navigation Satellite System (GNSS), inclinometers, crack

* Corresponding author.
E-mail address: hu.xie@pku.edu.cn (X. Hu).

https://doi.org/10.1016/j.rse.2021.112664
Received 6 August 2020; Received in revised form 30 June 2021; Accepted 18 August 2021
Available online 1 September 2021

gauges, and acoustic sensors (e.g., Smith and Dixon, 2015; Li L. et al., 2020, Li Y. et al., 2020; Xu et al., 2020). Steep and rugged topography makes the sensor installation and continuous monitoring extremely challenging. The non-contact remote sensing observations, such as high-resolution optical imagery, Light Detection and Ranging (LiDAR) survey, and Synthetic Aperture Radar (SAR) imagery, have been increasingly used to map the spatially continuous and regularly sampled surface displacements in active slopes (e.g., Booth et al., 2013; Chen et al., 2006; Hilley et al., 2004; Hu et al., 2019; Intrieri et al., 2020; Shi et al., 2019a). The above-mentioned area-based tools can generate digital elevation models (DEMs) and vertical displacements from their differential point cloud data (e.g., Kayen et al., 2006; Collins et al., 2009). Ground-based radar and LiDAR are now routinely used to monitor active slopes in mining and other geotechnical applications (e.g., Rouyet et al., 2017; Ventura et al., 2011). However, these measurements are rarely available until a specific project is initiated. The challenge is obtaining prior temporal data with sufficient spatial resolution to discern ground movements without the need for ground-based measurements.

The introduction of satellite-based SAR imagery with near-global coverage in the early 1990's has created the opportunity to obtain temporal SAR data going back almost three decades. SAR is composed of the phase and amplitude of microwave electromagnetic waves and enables us to measure ground displacements at millimeter accuracy and surface elevation at meter accuracy (Bürgmann et al., 2000; Jiang et al., 2017). The traditional Interferometric SAR (InSAR) analysis, utilizing the phase component, measures ground displacements in radar range direction (a.k.a., line-of-sight, LOS; range and LOS are used interchangeably). As a complement, the phase-based split-bandwidth interferometry and the amplitude-based pixel offset tacking methods provide two-dimensional displacements in radar range and azimuth directions. The accuracy of the split-bandwidth interferometry method is better than that of the amplitude pixel offset tracking when a sufficient correlation is maintained. To be specific, the standard deviation of azimuth split-bandwidth interferometry is ~0.1 m. In comparison, pixel offset tracking is 0.12–0.15 m when the coherence is 0.4 for C-band ERS data with a single-look azimuth pixel spacing of 12.5 m (Bechor and Zebker, 2006). A complete three-dimensional (3D) displacement field can be resolved by combining measurements from multiple SAR datasets and methods.

In this study, we focused on the Guobu slope on the bank of the reservoir of the Laxiwa hydropower station (China) (Fig. 1). Although a large headscarp of a preexisting rockslide was identified in the site investigation, the rockslide was deemed inactive and unlikely to pose a threat of reactivation (Xia et al., 2018). However, during the first filling of the reservoir in 2009, this rockslide, hereafter referred to as the Guobu slope, reactivated and started moving into the reservoir. Since then, the operators extended a major effort to monitor the slope and investigate the modes of instability (e.g., Lin et al., 2016; Xia et al., 2018).

Here we derived the 3D surface displacements and temporal behavior of the Guobu slope using azimuth and range InSAR results from two high-resolution TerraSAR-X tracks (2015–2017) and one moderate-resolution Sentinel-1 track (2016–2019). We identified a temporal long-wavelength correlation between the river level variations and the previously GPS-observed slope movements before 2014 and a subsequent seasonal correlation between the rainfall and landslide speed during 2015–2019. It suggests that while the initial rockslide movement mainly responded to reservoir filling, once the reservoir level stabilized there were continued surface motions modulated by precipitation. We also constrained the hydraulic diffusivity (1.05×10^{-7} m^2/s) and inferred the base of the movement (~200 m depth) from temporal and spatial surface movements.

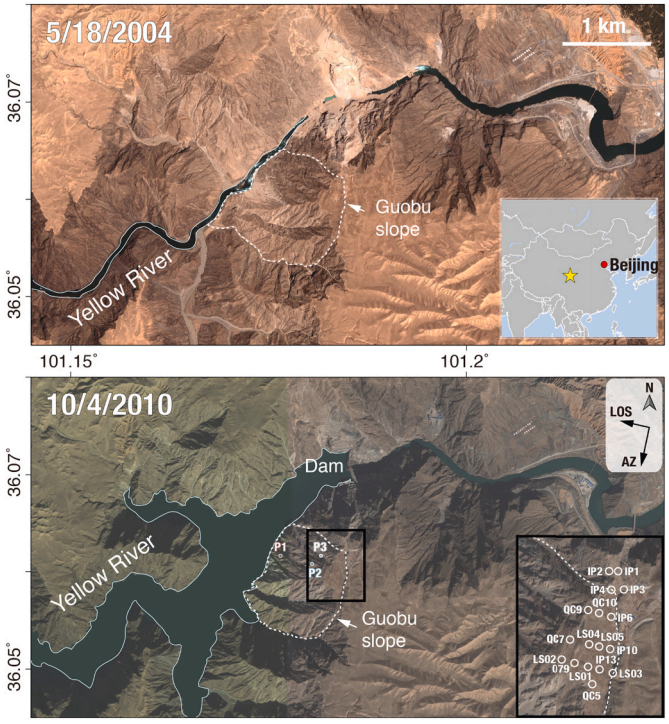

Fig. 1. Landscape of the Laxiwa hydropower station and Guobu slope in Qinghai, China. Two satellite images, one obtained by Quickbird on 5/18/2004 and the other obtained by Geoeye-1 on 10/4/2010, were collected before and after the first impoundment on 3/1/2009. The white dashed polygons outline the margins of the Guobu slope. Light blue lines delineate the Yellow River channels. Targets P1, P2 and P3 are selected for the time-series analysis in Figs. 5 and 7. The middle-right inset shows the trajectory of descending SAR satellites with azimuth direction (i.e., flight direction) and line-of-sight (LOS; i.e., range) direction indicated by arrows. The black-box inset shows the locations of 17 GPS sites deployed over the head of the slope. Fig. 6 shows the GPS time series. (For interpretation of the references to colour in this figure legend, the reader is referred to the web version of this article.)

1.1. Background and history of the study area

The upper reaches of the Yellow River occupy a deeply incised valley, making it an ideal site for high arc dams. More than twenty hydropower stations were constructed on the Yellow River to meet an ever-increasing demand for electricity. The Laxiwa hydropower station is a cascade power station from Longyang Gorge to Qingtong Gorge. The first impoundment was completed in March 2009, and the water level increased from 2,250 to 2,340 m above sea level (a.s.l.). Subsequently, the water level was successively raised to 2,400, 2,430, and 2,448 a.s.l. in February 2010, February 2011, and September 2012, respectively. The water level remained relatively stable at 2,448 m from September 2012 to May 2015 and then was allowed to rise to the design level of 2,452 m by the end of October 2015 and has remained stable thereafter (Li et al., 2019). Concurrently, the river channels widened from ~70 m to ~500 m (Fig. 1), and as a result of the reservoir impoundment, three slopes, including the Guobu slope, started to move (Shi et al., 2019b). While two of the slopes sit approximately 4 km and 8 km upstream of the dam, moving at rates of 40– 60 mm/yr during 2015–2018 (Shi et al., 2019b), the larger and faster Guobu slope, only about 1-km southwest of the Laxiwa hydropower station, has drawn immediate attention as a threat to the dam, its powerhouse, and the residential community ~4 km downstream. The Guobu slope is a large toppling rock failure (Lin et al., 2016; Xia et al., 2018). The slope is composed of Mesozoic, medium- to coarse-grained, and highly jointed granite. Loose Quaternary deposits cover the slope and platform to a depth of ~1–11 m (Lin et al., 2016) and are subject to erosion by rain and wind. While the joints are wide open in

surface exposures, at depth the unweathered granite is compact, and the joints are more tightly closed. Exposures in exploration tunnels also show preexisting shears with slickenside surfaces coated with clay infill. The presence of a well-developed, steeply dipping joint set striking parallel to the river gorge trend makes the Guobu slope highly vulnerable to toppling (Lin et al., 2016).

1.2. Previous work

While the area was identified as an ancient landslide during a geological survey in 1989 before the dam construction (Xia et al., 2018), monitoring data from simple observation monuments between 1991 and 1997 reported no evidence of displacement (Xia et al., 2018). A retaining dam and a drainage ditch were constructed near the headscarp of the slope in 2004 to divert rainwater from infiltrating into the slope (Wang, 2011); however, the drainage ditch was destroyed in 2005 (Zhang, 2014). Thereafter, rainwater would be able to seep into the Guobu slope easily. Optical remote sensing data suggested an extension of the headscarp during 2005 (Xia et al., 2018). The present-day vertical scarp at the top of the slide is more than 30 m high, and the estimated submerged depth at the toe is 200 m. The elevation difference between the river surface after the impoundment and the uppermost part of the headscarp is as much as 500 m (Fig. 2).

The fastest episodes of slide movements occurred immediately after the first impoundment of the reservoir in 2009 (Zhang, 2014). A total of 17 Global Positioning System (GPS) stations were immediately installed in the headscarp area (black box inset in Fig. 1) to monitor the slope movements in eastward (E), northward (N) and upward (U) directions (Lin et al., 2016; Xia et al., 2018). Here we extracted the time-series displacements measured from August 2009 to December 2013 reported in Zhang (2014). The accelerated deformation at the Guobu slope was distributed along the preexisting joints (Lin et al., 2016), reaching as much as 40 m (e.g., $\sqrt{E^2+N^2+U^2}$at GPS site QC7) from 2009 to July 2014 (Xia et al., 2018). Eventually, in response to gradually stabilized water level, the landslide speed slowed down to ~0.8 m/yr from late 2015 to April 2017, according to InSAR observations (Li et al., 2019).

Previous slope monitoring using SAR imagery (e.g., Shi et al., 2017b; Li et al., 2019) mainly focused on the displacement mapping and identified an overall decelerating trend. Limited by the quantity and temporal resolution of SAR imagery and the traditional methods of InSAR and pixel offset tracking, only qualitative interpretations were achieved.

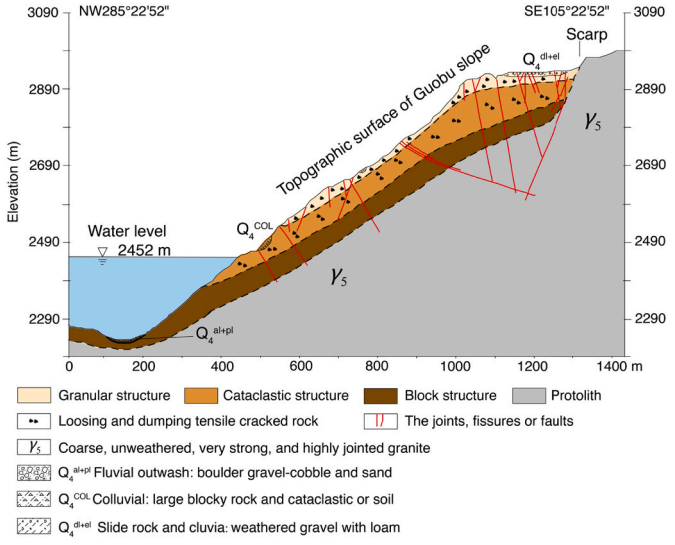

Fig. 2. Geological cross-sections of the Guobu slope. The dashed lines show the inferred limits of different zones, modified from Lin et al., 2016 and Shi et al., 2017b.

2. InSAR measurements

2.1. Conventional and split-bandwidth InSAR methodology

We relied on three descending datasets, two high-resolution TerraSAR-X spotlight tracks (TSX-74 and TSX-150) and one Sentinel-1 track (S1-33), to measure the spatiotemporal displacements of the Guobu slope. The average acquisition intervals are ~22 days and ~12 days for TerraSAR-X and Sentinel-1 datasets, respectively (Table 1 and Fig. 3). Due to steep slopes, geometric distortions such as the foreshortening and layover occurred in ascending tracks for steep Guobu slope facing toward the oncoming radar pulses. Therefore, the descending orbital SAR data are the only applicable spaceborne SAR observations at the Guobu slope.

We applied different data processing strategies to derive the surface displacements for Sentinel-1 and TerraSAR-X datasets, whose pixel spacing, temporal intervals, and electromagnetic wavelength are different (Table 1).

For the Sentinel-1 track, we used the standard time-series InSAR method to obtain LOS displacements. We applied multi-look factors of 4 by 1 in range and azimuth and Goldstein filters with a 16 × 16-pixel window to enhance the signal-to-noise ratio. Pixels with coherence larger than 0.3 were considered for phase unwrapping. The least-squares estimation resolved the topographic errors on a set of interferograms based on a mathematical relationship with the satellite perpendicular baseline (e.g., Shi et al., 2017b). We corrected the long-wavelength atmospheric phase screen by removing a linear ramp fitted by radar azimuth and range positions and surface elevation (Liao et al., 2013). Time-series displacements were solved by the singular value decomposition of a total of 84 interferograms.

The employment of traditional time-series InSAR method using TerraSAR-X data with longer temporal baselines and short electromagnetic wavelength in our study area is challenged by the phase unwrapping errors (Li et al., 2019). On the other hand, the time-series split-bandwidth interferometry reduces the sensitivity of phase to displacements, and thus phase unwrapping becomes much easier (Jiang et al., 2017; Shi et al., 2017a). We opted for a time-series split-bandwidth interferometry method to extract the two-dimensional azimuth and LOS displacements of the Guobu slope. In contrast, the traditional InSAR method can only resolve the one-dimensional LOS displacements. The split-bandwidth interferometry extracts the ground motions from the differential phase between the forward- and backward-looking interferograms (Bechor and Zebker, 2006; Jiang et al., 2017). All scenes are co-registered to the common reference imagery (9/27/2016 for TSX-74 and 10/2/2016 for TSX-150) using auxiliary information from Shuttle Radar Topography Mission (SRTM) DEM and precise orbits. The DEM-assisted co-registration can remove the phase component correlated with topography and baselines in the range split-bandwidth interferometry (Sansosti et al., 2006). The resampled image m_i is split into two low-resolution sub-looking images $m_i^f$and m_i^b by filtering out the forward and backward bands in the frequency domain, and the procedure is applied for the azimuth and range directions, respectively. The theoretically optimum bandwidth in our study is 1/3rd of the

Table 1
SAR data parameters.

Sensor	TerraSAR-X		Sentinel-1A/B
Orbit number	74	150	33
Orbit direction	Descending	Descending	Descending
Heading angle (°)	189.6	191.0	193.1
Look angle (°)	37.9	22.8	32.6
Pixel spacing (m; Range × Azimuth)	0.45 × 0.86		2.33 × 13.97
Timespan	9/2015–4/2017	12/2015–4/2017	1/2016–7/2019
Number of scenes	18	16	85

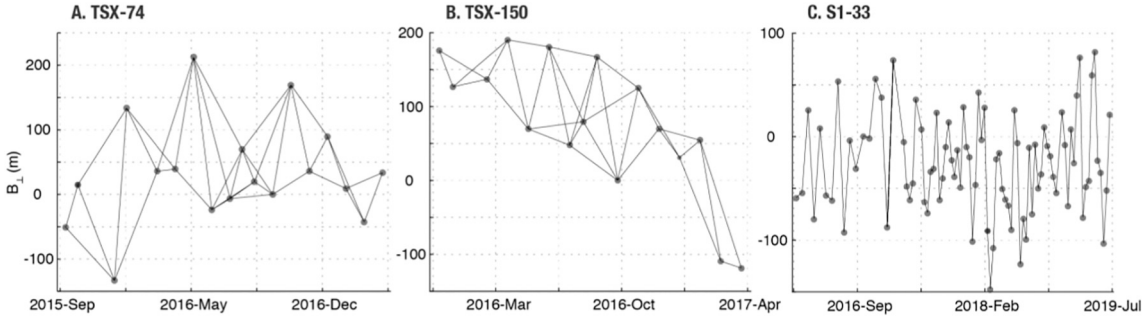

Fig. 3. InSAR image pairs. (A) TSX-74, (B) TSX-150, and (C) Sentinel-1 (S1–33).

original signal (Bamler and Eineder, 2005; De Zan, 2011). Image pairs with temporal baselines less than 80 days are used to generate interferograms. The forward- and backward-looking interferograms are formed by the corresponding sub-look images with a multi-look factor of 5 in both range and azimuth directions. The consequent range or azimuth differential interferograms can be directly produced from the conjugate multiplication of the forward- and backward-looking interferograms. Goldstein filters are incorporated to form the forward−/backward-looking interferograms and differential interferograms. Pixels with the coherence larger than 0.3 in the differential interferograms are selected as reliable inputs for phase unwrapping in temporal and spatial domains (Hooper and Zebker, 2007) for the time-series analysis.

$$\Delta d = \frac{\phi_{\text{split}}}{2\pi\Delta f_c} F \cdot p \tag{1}$$

where Δd is the ground displacement, ϕ_{split} is the differential phase in the azimuth and range directions, Δf_c is the spectral separation between the forward- and backward looking interferograms which equals 2/3 of the bandwidth in our study, F is the sampling frequency corresponding to about 3.3×10^8 MHz in range and 8,100 Hz in azimuth, and p is the pixel spacing. When applying the TerraSAR-X data, one phase cycle amounts to 0.75- and 1.46-m ground displacements along with the range and azimuth via the split-bandwidth interferometry, respectively.

2.2. The 3D displacement solutions

The extracted LOS and azimuth displacements are the projections of 3D displacements on the corresponding directions. The relationship between InSAR measurements and 3D displacements is given by,

$$\begin{cases} d_N sin\alpha sin\theta - d_E cos\alpha sin\theta + d_U cos\theta = d_{LOS} + \delta_{LOS} \\ d_N cos\alpha + d_E sin\alpha = d_{AZ} + \delta_{AZ} \end{cases} \tag{2}$$

where d_N, d_E, d_U are displacements measured in the north, east, and vertical directions, respectively; α is the satellite heading angle; θ is the nominal incidence angle; d_{LOS} and d_{AZ} are the observed LOS and azimuth displacements; δ_{LOS} and δ_{AZ} are the corresponding observation errors.

Although all datasets are from descending orbits, their divergent look angles allow us to resolve 3D displacement fields (Figs. S1 and S2). Each individual LOS and azimuth displacement maps are interpolated to 30-by-30 m grids for colocation. We can establish 5 equations with 3 unknowns d_N, d_E, d_U through Euler rotations.

$$\begin{bmatrix} sin\alpha^{t74} sin\theta^{t74} & -cos\alpha^{t74} sin\theta^{t74} & cos\theta^{t74} \\ cos\alpha^{t74} & sin\alpha^{t74} & 0 \\ sin\alpha^{t150} sin\theta^{t150} & -cos\alpha^{t150} sin\theta^{t150} & cos\theta^{t150} \\ cos\alpha^{t150} & sin\alpha^{t150} & 0 \\ sin\alpha^{s33} sin\theta^{s33} & -cos\alpha^{s33} sin\theta^{s33} & cos\theta^{s33} \end{bmatrix} \begin{bmatrix} d_N \\ d_E \\ d_U \end{bmatrix} = \begin{bmatrix} d_{LOS}^{t74} \\ d_{AZ}^{t74} \\ d_{LOS}^{t150} \\ d_{AZ}^{t150} \\ d_{LOS}^{s33} \end{bmatrix} + \begin{bmatrix} \delta_{LOS}^{t74} \\ \delta_{AZ}^{t74} \\ \delta_{LOS}^{t150} \\ \delta_{AZ}^{t150} \\ \delta_{LOS}^{s33} \end{bmatrix} \tag{3}$$

where the superscripts $t74$, $t150$ and $s33$ indicate measurements from TSX-74, TSX-150, and Sentinel-1, respectively. A diagonal matrix determined by the reciprocal standard deviation of each measurement in Li et al. (2019) can be used as the weight matrix to integrate measurements at different precisions (Hu et al., 2014). The 3D displacements are solved by the least-squares estimation using multi-dimensional LOS and azimuth displacements from Sentinel-1 and TerraSAR-X data.

2.3. Hydraulic diffusivity inversion

Rainwater recharge modulates the subsurface pore pressure, frictional strength, and landslide rates. Transient pore pressure changes from the surficial water input can be characterized by one-dimensional diffusion model (Terzaghi et al., 1996).

$$\frac{dP}{dt} = D\frac{d^2P}{dz^2} \quad t > 0, z > 0 \tag{4}$$

where P is the pore pressure, t is time, D is the characteristic hydraulic diffusivity, and z is the depth to the basal plane. This model captures the first-order pore pressure propagation to a certain distance below the ground surface.

The rainwater recharge $R(t)$ is a proxy for the transient pore pressure at the surface ($z = 0$).

$$P = r \cdot R(t) \quad z = 0 \tag{5}$$

where r is a scaler that relates the water to pressure. This process is analogous to the conductive heat transfer. The analytical solution is given by (Carslaw and Jaeger, 1947)

$$P(z,t) = \frac{z}{2\sqrt{\pi D}} \int_0^t \frac{e^{-\frac{z^2}{4D(t-s)}}}{\sqrt{(t-s)^3}} P(s, z=0) ds \tag{6}$$

where s is a time variable. We obtained the daily precipitation data (Station ID: 52868, location: 36°01′ N, 101°22′ E) to infer the pore pressures at given depth and hydraulic diffusivity that can best correlate with SAR-derived time-series landslide speed.

3. Results

We computed two azimuth displacements and three LOS displacements from Sentinel-1 and TerraSAR-X data sets (Fig. S1). Since the viewing directions of the three datasets are almost parallel to the slope orientation (Fig. 1), the displacements of the Guobu slope can be readily detected in LOS measurements. In contrast, the displacements in the azimuth direction are mainly correlated with the local slope variations. The 3D displacements are recovered with measurements from the range and azimuth interferometry (Fig. 4). For most low-gradient landslides, the vertical rates are generally a couple of orders of magnitude less than those in the horizontal direction. Here at the Guobu slope, it is remarkable that the vertical rates are in a comparable order of

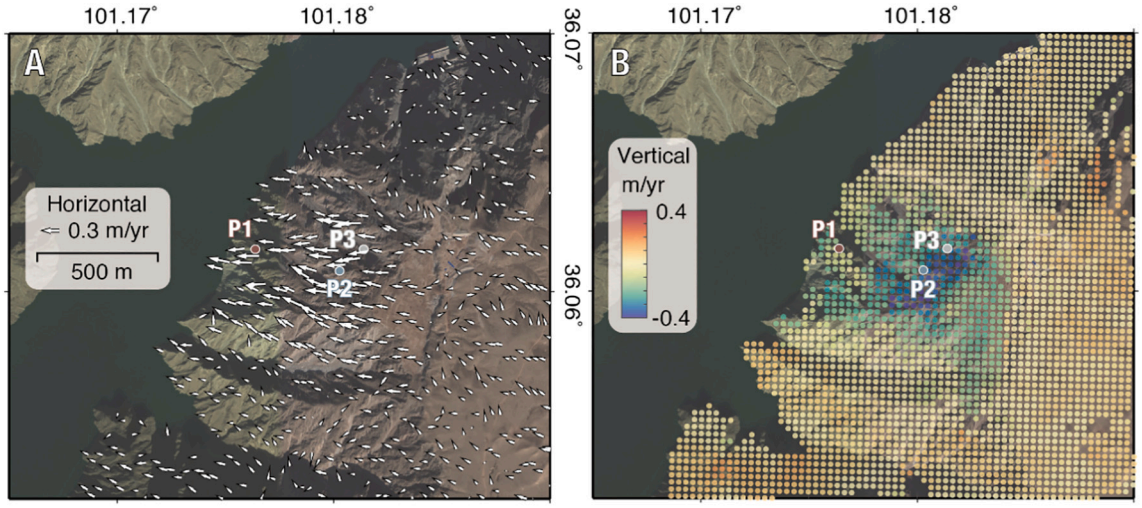

Fig. 4. 3D displacement velocity maps of the Guobu slope. (A) The horizontal and (B) the vertical velocities. InSAR-derived displacements of P1-P3 targets are shown in Figs. 5 and 7.

magnitude to that of the horizontal rates due to the oversteepened slope. The fastest rates of movement occur in the middle section (~0.4 m/yr in the vertical and ~0.7 m/yr in the horizontal). Similar phenomenon has been observed in other steep slopes, e.g., the Baige landslide moving at similar rates of ~0.1 m/day in both vertical and horizontal directions between August 2017 and February 2018, prior to damming the Jinshajiang River on October 10th 2018 (Li L. et al., 2020, Li Y. et al., 2020); the Shuping landslide moving at 0.6–0.8 m/yr in both vertical and horizontal directions from February 2009 to April 2010 (Shi et al., 2015); the La Valette landslide moving at up to 11 m/yr vertically and 20 m/yr horizontally during April–November 2010 (Raucoules et al., 2013). The active slope surface mainly moves horizontally to the west (Fig. 4A). Both the horizontal and vertical rates of movement below the headscarp decrease from top to bottom. There are also a few targets in the lower portion showing minor uplift, which might be due to mass accumulation.

We selected three targets (P1-P3 in Figs. 1B and 4) for time-series displacement analysis. P1 is located at the lower part of the Guobu slope, and P2 and P3 are located in the most deforming area below the headscarp. We extracted their LOS displacements from the mean of all measurements within 60 m, and the error bars in Fig. 5 represent one standard deviation for each track. The error bars of the TerraSAR-X measurements are larger than that of the Sentinel-1 due to a different accuracy between split-bandwidth interferometry and the conventional InSAR ranging mapping. We then projected the LOS time series of different tracks into the downhill direction to constitute the time series with enhanced temporal resolution (Fig. 5). Good consistency in the downslope displacements from independent datasets cross-validates our InSAR results. The cumulative downslope movements reach >3.5 m from late 2015 to mid-2019 with a peak-to-peak seasonal amplitude of ~0.15 m.

4. Discussion

4.1. Correlation between GPS-observed time-series displacements and reservoir water level before 2014

Large rapid water level changes can destabilize the slopes in reservoir areas (Paronuzzi et al., 2013; Qi et al., 2004). We extracted the 3D observations from 17 GPS stations around the headscarp (black box inset in Fig. 1) that have been reported in Zhang (2014) and used the absolute value, i.e., $\sqrt{E^2+N^2+U^2}$, to characterize the landslide motions (Fig. 6). The largest measured displacements, >40 m in 4.5 years, occurred at GPS location QC7 located on top of a toppling block on the downslope edge of the bench formed at the top of the slide (Figs. 1 and 6C). In comparison, along the northern flank of the headscarp, points IP1-IP4, moved on the order of 5 m in the same 4.5-year period (Figs. 6C) (Zhang, 2014). The landslide rate changes (up to 80–90 mm/day) were in sync with the water levels. The rates decreased to less than 5 mm/day when the water levels became generally stable at ~2,448 m a.s.l between September 2012 and July 2014, during the observation period (Xia et al., 2018). To investigate the slope movements in response to water level changes, we focused on the time span between June 2011 and November 2013 when water levels stabilized gradually (Figs. 6B, D), and we extracted the non-linear components for both water levels and displacements. Unlike the pronounced seasonal variation in InSAR-derived displacement during late 2015 to mid-2019, the slope movement did not exhibit seasonal deformation before the reservoir water level stabilized (Fig. 6D). We cannot rule out the possibility of a seasonal component in GPS observations, yet the amplitude is apparently insignificant compared to the drastic long-term rates during water impoundment period. Remarkably, the cross-correlation result shows that the non-linear water level changes and deformation are perfectly in phase with a zero-day shift, suggesting that the slope stability was entirely subject to water level changes in the reservoir and the impact from the precipitation was negligible during this period.

4.2. Correlation between the InSAR-derived seasonal displacements and rainfall during 2015–2019

Seasonal variations in the rate of movement due to the hydro-mechanically coupling associated with the precipitation have been documented in rockslides (e.g., Brückl et al., 2013; Crosta et al., 2017; Fig. 5). We focused on the relationship between precipitations and slope displacements to better understand the driving mechanisms while the water level remained essentially unchanged during 2015–2019.

Our data show that the fastest displacements occur in the rainy season from June to September as observed by comparing the daily precipitation (vertical stems in Fig. 7A) and smoothed record from the daily average displacements on a 30-day running window (continuous blue line in Fig. 7A). Generally, the rate peaks when the annual cumulative precipitation reaches at least 150 mm (black dashed line in Fig. 7A). On the other hand, the lowest rates occur between January and March, consistent with the decrease seasonal rainfall (Fig. 7). The rainwater can easily infiltrate into the Guobu slope through the multitude of joints from the slope surface. To further quantify the role of precipitation in controlling the landslide velocity, we simulated the

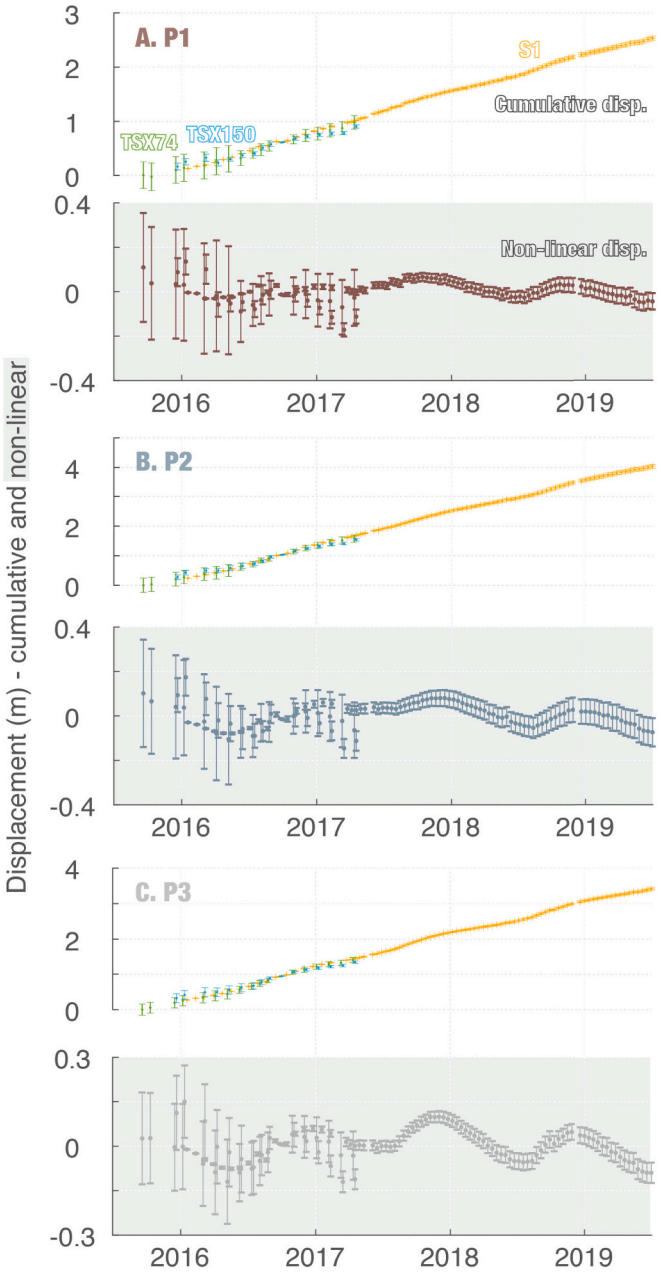

Fig. 5. InSAR-derived time-series cumulative and non-linear/seasonal displacement of three selected targets (locations shown in Figs. 1B and 4) – (A) P1, (B) P2, and (C) P3. Green, blue and yellow symbols are TerraSAR-X (TSX) and Sentinel-1 (S1) results, respectively. Time series in the gray boxes are the non-linear components. Error bars represent one standard deviation of the measurements within 60-m-distance to the given target. (For interpretation of the references to colour in this figure legend, the reader is referred to the web version of this article.)

time-dependent pore pressures at a characteristic depth of 200 m using the one-dimensional diffusion model (section 3.3). The minimum residual between the modeled pore pressure and InSAR-measured downhill movements help constrain a hydraulic diffusivity of ~1.05×10^{-7} m^2/s.

4.3. Inferred depth of movement

Landslide depth and volume are critical parameters to evaluate and mitigate potential failures. However, quantifying the basal geometry at the Guobu slope from traditional borehole drilling or tunnel excavation is challenging due to rapid initial deformation, risky field survey conditionsdue to the steepness of the slope, and high-strength materials. Lin et al. (2016) reported a rough estimation on the volume to be on the order of 3×10^7 m^3, from boreholes and tunnels at a few locations over the less deforming slope margins.

The 3D surface displacements can be used to invert the basal geometry following the law of mass conservation (Booth et al., 2013; Intrieri et al., 2020; Hu et al., 2018; Hu et al., 2019). However, the mass conservation approach can hardly be applied to the Guobu slope because we lack the displacement measurements on the submerged toe of the slope. Therefore, we employed a vector inclination method (Carter and Bentley, 1985) to infer the basal surface of the Guobu slope along cross-section profiles. This method has been used to characterize the translational, planar, or rotational landslides based on the field-based displacement measurements (Carter and Bentley, 1985) and InSAR-derived 3D displacements (Intrieri et al., 2020). The fundamental assumption is that the rock mass moves as a rigid body in an infinitesimal distance so that the vectors of surface movements are parallel to the continuous sliding surfaces underneath. The basal surfaces results are determined by the position and direction of the applied surface vectors. As revealed by the InSAR derived 3D measurements, the upper part of the Guobo slope is a large, complex rock topple that may have some joints and shears at depth along which there is sliding. However, multiple basal surfaces have been considered in previous numerical analysis (Lin et al., 2016). Using the vector inclination approach, we derived the slip surfaces for cross-section AA' and BB' (locations are shown in the inset of Fig. 8 and Fig. S1A) using our 3D displacements. The maximum and average vertical distance from the surface to the inferred base surfaces are 227_{+26}^{-21} and 150 m along AA', and 224_{+35}^{-28} and 135 m along BB'; the stratigraphic depth is 168_{+23}^{-16} and 149_{+23}^{-11} m along AA' and BB', respectively (Fig. 8). The largest landslide thickness and the most extensive surface displacements occur between elevation 2,700 m and 2,800 m in the longitudinal middle of the slope. Correspondingly, we estimated the landslide volume to be on the order of 10^7 m^3, in a general agreement with previous reports (Lin et al., 2016; Xia et al., 2018).

4.4. Envisions

Our framework can be employed in other study areas. Multi-temporal InSAR scheme can effectively suppress the random noise and improve the performance of conventional split bandwidth InSAR. Jo et al. (2015) reported the accuracy of stacking split bandwidth InSAR in the azimuth direction to be about 10.7 and 10.3 mm/yr in Kīlauea Volcano, Hawai'i when using the ascending and descending ENVISAT ASAR tracks. The root-mean-square error of the stacking approach has decreased by six times compared to the conventional split bandwidth InSAR method (Jo et al., 2015). In addition, natural environments are usually featured with distributed scatterers with low phase stabilities such as in the vegetated areas. SqueeSAR method seeks the statistical characteristics of homogeneous pixels and significantly increases the density of credible pixels, especially for the non-urban environments such as debris slides (Ferretti et al., 2011; Shi et al., 2018). Beyond that, analytical and numerical models can be incorporated to infer the basal geometries and physical properties of landslide systems based on remotely sensed surface displacements of the entire active catchment (e.g., Booth et al., 2013; Hu et al., 2018; Hu et al., 2019; Nikolaeva et al., 2014).

5. Concluding remarks

We obtained 3D surface velocities and the time-dependent downslope movements of the Guobu slope in response to river level changes (before 2014) and seasonal precipitation (2015–2019) from a joint analysis of azimuth and range InSAR observations from TerraSAR-X and Sentinel-1 satellites, previously reported GPS observations (Zhang,

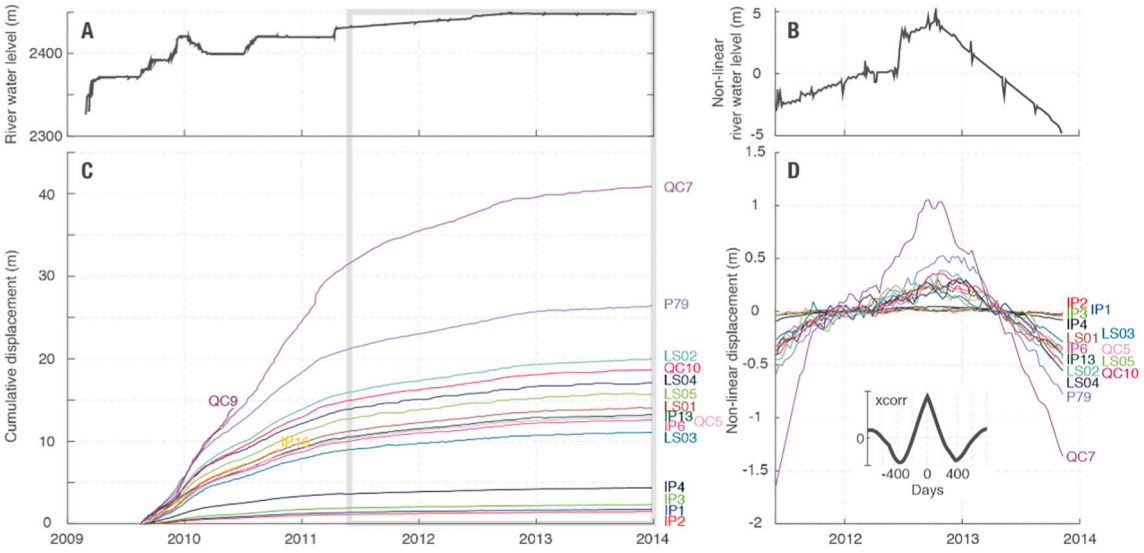

Fig. 6. River level and GPS-derived time-series displacements during 2009–2014. The locations of the GPS sites are marked in Fig. 1B. (A) The river level during 2009–2013 and (B) its non-linear component from June 2011 to November 2013 when the water level became stable gradually. (C) The displacements during 2009–2013 of 17 GPS sites and (D) their non-linear component of 15 GPS sites from June 2011 to November 2013 (IP10 and QC9 are excluded as no observation during this time frame). GPS data were extracted from Zhang (2014). The inset in panel D shows the cross-correlation (xcorr) between the non-linear river level and the average non-linear displacement of GPS stations at 11 stations with evident high-frequency signals (IP1 to IP4 are excluded); results are completely in phase with zero-day shift.

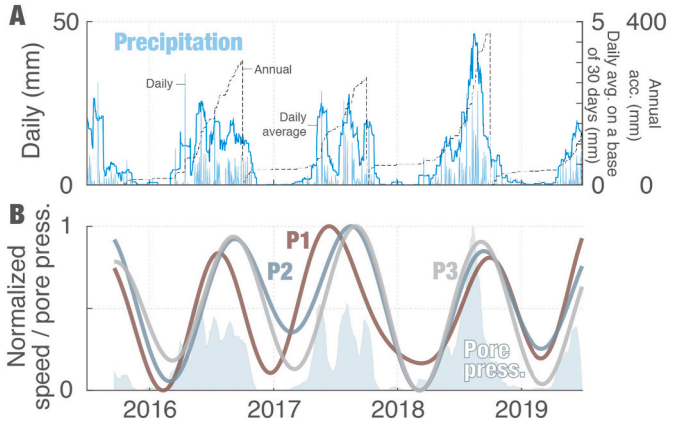

Fig. 7. Landslide speed, precipitation, and the inferred pore pressure. (A) Daily precipitation in vertical stems, daily average precipitation on a 30-day running window in blue line, and annual cumulative precipitation (reset to 0 in each October 1st) in black dashed line. (B) The normalized estimates of landslide speed at three targets P1-P3 (Figs. 4 and 5) and pore pressure at a characteristic distance of 200 m below the surface. (For interpretation of the references to colour in this figure legend, the reader is referred to the web version of this article.)

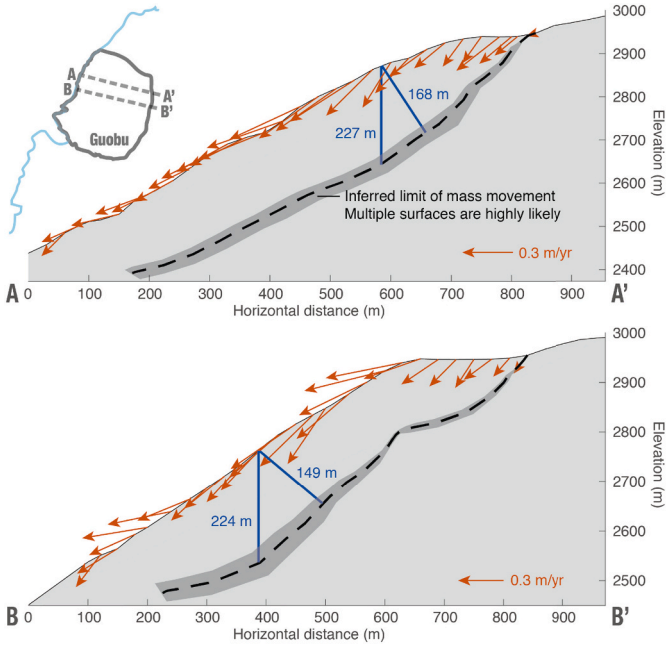

Fig. 8. Slope cross sections AA' and BB'. Arrows denote the surface displacement vectors in the indicated magnitude and directions. Dashed lines show the inferred limit of mass movement from the surface displacement vectors. Gray shades show the uncertainties derived from one standard deviation of displacements within a 30-m distance to the selected targets. We noted that multiple shear surfaces and joints are highly likely.

2014), and the hydroclimatic record of reservoir water levels and precipitation. The results show that the middle part of the Guobu slope moves fastest where the slope steepens. Before the river level became stable from roughly 2012 to early 2015, the activity of the Guobu slope was controlled by the water level changes without temporal delay, suggesting very high fracture permeability of the lower portion of the rock mass. Thereafter, the landslide motions have been synchronous with the seasonal rainfall with a peak rate of movement between June and September. By correlating the rainfall-modulated pore pressure and landslide speed, we estimated the hydraulic diffusivity of the rockslide mass to be $\sim 1.05 \times 10^{-7}$ m^2/s, which is in the typical range for fractured rocks. A first-order approximation of the basal slip vectors inferred from 3D surface displacement vectors gives a depth of mass movement ~200 m and a corresponding landslide volume on the order of 10^7 m^3. These metrics can help better prepare for potential co-/post-failure inundation and flooding. More importantly, our results demonstrate that the slope continues to move, though at a reduced rate than during the reservoir filling. Therefore, continued monitoring of the rock mass is critical for detecting any tendency for slide acceleration and the potential for increased instability.

Author statement

X.S. and X.H. designed the study. X.S., H.J., and X.W. analyzed SAR imagery. X.H. performed the modeling. X.H., X.S., N.S., R.K. and S.Q. interpreted the results. L.Z. provided TerraSAR-X data. X.S. and X.H. drafted the paper with input from all co-authors.

Declaration of Competing Interest

The authors declare that they have no known competing financial interests or personal relationships that could have appeared to influence the work reported in this paper.

Acknowledgement

This work was financially supported by the National Natural Science Foundation of China (Grant No. 41702376, 41774006, and 41825018) and the Second Tibetan Plateau Scientific Expedition and Research Program (STEP) (Grant No. 2019QZKK0904). The TerraSAR-X datasets were provided by German Aerospace Center (DLR) through the TerraSAR-X AO projects (GEO2520 and GEO3353). The Copernicus Sentinel-1 data were provided by European Space Agency (ESA) and downloaded from the Alaska Satellite Facility (ASF).

Appendix A. Supplementary data

Supplementary data to this article can be found online at https://doi.org/10.1016/j.rse.2021.112664.

References

Bamler, R., Eineder, M., 2005. Accuracy of differential shift estimation by correlation and split-bandwidth interferometry for wideband and delta-k SAR systems. IEEE Geosci. Remote Sens. Lett. 2, 151–155.
Bechor, N.B., Zebker, H.A., 2006. Measuring two-dimensional movements using a single InSAR pair. Geophys. Res. Lett. 33, L16311.
Booth, A.M., Lamb, M.P., Avouac, J.P., Delacourt, C., 2013. Landslide velocity, thickness, and rheology from remote sensing: La Clapière landslide, France. Geophys. Res. Lett. 40, 4299–4304.
Brückl, E., Brunner, F.K., Lang, E., Mertl, S., Müller, M., Stary, U., 2013. The Gradenbach Observatory—monitoring deep-seated gravitational slope deformation by geodetic, hydrological, and seismological methods. Landslides 10, 815–829.
Bürgmann, R., Rosen, P.A., Fielding, E.J., 2000. Synthetic aperture radar interferometry to measure Earth's surface topography and its deformation. Annu. Rev. Earth Planet. Sci. 28, 169–209.
Carslaw, H.S., Jaeger, J.C., 1947. Conduction of Heat in Solids. Clarendon Press.
Carter, M., Bentley, S.P., 1985. The geometry of slip surfaces beneath landslides: predictions from surface measurements. Can. Geotech. J. 22, 234–238.
Chen, R.-F., Chang, K.-J., Angelier, J., Chan, Y.-C., Deffontaines, B., Lee, C.-T., Lin, M.-L., 2006. Topographical changes revealed by high-resolution airborne LiDAR data: the 1999 Tsaoling landslide induced by the chi–chi earthquake. Eng. Geol. 88, 160–172.
Chen, T., Deng, J., Sitar, N., Zheng, J., Liu, T., Liu, A., Zheng, L., 2017. Stability investigation and stabilization of a heavily fractured and loosened rock slope during construction of a strategic hydropower station in China. Eng. Geol. 221, 70–81.
Collins, B.D., Minasian, D., Kayen, R., 2009. Topographic change detection at select archeological sites in grand canyon National Park, Arizona, 2006-2007. US Geol. Surv. Sci. Investig. Rep. 2009–5116, 58 p.
Crosta, G.B., Agliardi, F., Rivolta, C., Alberti, S., Dei Cas, L., 2017. Long-term evolution and early warning strategies for complex rockslides by real-time monitoring. Landslides 14, 1615–1632.
De Zan, F., 2011. Coherent shift estimation for stacks of SAR images. IEEE Geosci. Remote Sens. Lett. 8, 1095–1099.
Ferretti, A., Fumagalli, A., Novali, F., Prati, C., Rocca, F., Rucci, A., 2011. A new algorithm for processing Interferometric data-stacks: SqueeSAR. IEEE Trans. Geosci. Remote Sens. 49, 3460–3470.
Hilley, G.E., Bürgmann, R., Ferretti, A., Novali, F., Rocca, F., 2004. Dynamics of slow-moving landslides from permanent scatterer analysis. Science 304, 1952–1955.
Hooper, A., Zebker, H.A., 2007. Phase unwrapping in three dimensions with application to InSAR time series. J. Opt. Soc. Am. A 24, 2737–2747.
Hu, J., Li, Z.W., Ding, X.L., Zhu, J.J., Zhang, L., Sun, Q., 2014. Resolving three-dimensional surface displacements from InSAR measurements: a review. Earth Sci. Rev. 133, 1–17.
Hu, X., Lu, Z., Pierson, T.C., Kramer, R., George, D.L., 2018. Combining InSAR and GPS to determine transient movement and thickness of a seasonally active low-gradient translational landslide. Geophys. Res. Lett. 45, 1453–1462.
Hu, X., Bürgmann, R., Lu, Z., Handwerger, A.L., Wang, T., Miao, R., 2019. Mobility, thickness, and hydraulic diffusivity of the slow-moving Monroe landslide in California revealed by L-band satellite radar interferometry. J. Geophys. Res. Solid Earth 124, 7504–7518.
Intrieri, E., Frodella, W., Raspini, F., Bardi, F., Tofani, V., 2020. Using satellite interferometry to infer landslide sliding surface depth and geometry. Remote Sens. 12, 1462.
Jiang, H., Feng, G., Wang, T., Bürgmann, R., 2017. Toward full exploitation of coherent and incoherent information in Sentinel-1 TOPS data for retrieving surface displacement: application to the 2016 Kumamoto (Japan) earthquake. Geophys. Res. Lett. 44.
Jo, M.-J., Jung, H.-S., Won, J.-S., Poland, M., Miklius, A., Lu, Z., 2015. Measurement of slow-moving along-track displacement from an efficient multiple-aperture SAR interferometry (MAI) stacking. J. Geod. 89, 411–425.
Kayen, R., Pack, R.T., Bay, J., Sugimoto, S., Tanaka, H., 2006. Ground-LIDAR visualization of surface and structural deformations of the Niigata ken Chuetsu, 23 October 2005, earthquake. Earthquake Spectra 22 (S1), S147–S162.
Li, M., Zhang, L., Shi, X., Liao, M., Yang, M., 2019. Monitoring active motion of the Guobu landslide near the Laxiwa Hydropower Station in China by time-series point-like targets offset tracking. Remote Sens. Environ. 221, 80–93.
Li, M., Zhang, L., Ding, C., Li, W., Luo, H., Liao, M., Xu, Q., 2020. Retrieval of historical surface displacements of the Baige landslide from time-series SAR observations for retrospective analysis of the collapse event. Remote Sens. Environ. 240, 111695.
Li, Y., Utili, S., Milledge, D., Chen, L., Yin, K., 2020. Chasing a complete understanding of the failure mechanisms and potential hazards of the slow moving Liangshuijing landslide. Eng. Geol. 105977.
Liao, M., Jiang, H., Wang, Y., Wang, T., Zhang, L., 2013. Improved topographic mapping through high-resolution SAR interferometry with atmospheric effect removal. ISPRS J. Photogramm. Remote Sens. 80, 72–79.
Lin, P., Liu, X., Hu, S., Li, P., 2016. Large deformation analysis of a high steep slope relating to the Laxiwa reservoir, China. Rock Mech. Rock. Eng. 49, 2253–2276.
Müller-Salzburg, L., 1987. The Vajont catastrophe— a personal review. Eng. Geol. 24, 423–444.
Mulligan, M., van Soesbergen, A., Sáenz, L., 2020. GOODD, a global dataset of more than 38,000 georeferenced dams. Scientific Data 7, 31.
Nikolaeva, E., Walter, T.R., Shirzaei, M., Zschau, J., 2014. Landslide observation and volume estimation in Central Georgia based on L-band InSAR. Nat. Hazards Earth Syst. Sci. 14, 675–688.
Paronuzzi, P., Rigo, E., Bolla, A., 2013. Influence of filling–drawdown cycles of the Vajont reservoir on Mt. Toc slope stability. Geomorphology 191, 75–93.
Qi, S., Wu, F., Yan, F., Lan, H., 2004. Mechanism of deep cracks in the left bank slope of Jinping first stage hydropower station. Eng. Geol. 73, 129–144.
Qi, S., Zou, Y., Wu, F., Yan, C., Fan, J., Zang, M., Zhang, S., Wang, R., 2017. A recognition and geological model of a deep-seated ancient landslide at a reservoir under construction. Remote Sens. 9, 383.
Raucoules, D., de Michele, M., Malet, J.P., Ulrich, P., 2013. Time-variable 3D ground displacements from high-resolution synthetic aperture radar (SAR). Application to La Valette landslide (south French Alps). Remote Sens. Environ. 139, 198–204.
Rouyet, L., Kristensen, L., Derron, M.-H., Michoud, C., Blikra, L.H., Jaboyedoff, M., Lauknes, T.R., 2017. Evidence of rock slope breathing using ground-based InSAR. Geomorphology 289, 152–169.
Sansosti, E., Berardino, P., Manunta, M., Serafino, F., Fornaro, G., 2006. Geometrical SAR image registration. IEEE Trans. Geosci. Remote Sens. 44, 2861–2870.
Schuster, R.L., 1979. Reservoir-induced landslides. Bull. Int. Assoc. Eng. Geol. – Bull. l'Assoc. Int. Géol. l'Ingén. 20, 8–15.
Shi, G., Lin, H., Ma, P., 2018. A hybrid method for stability monitoring in low-coherence urban regions using persistent and distributed scatterers. IEEE J. Selec. Top. Appl. Earth Observ. Remote Sens. 11 (10), 3811–3821.
Shi, X., Zhang, L., Balz, T., Liao, M., 2015. Landslide deformation monitoring using point-like target offset tracking with multi-mode high-resolution TerraSAR-X data. ISPRS J. Photogramm. Remote Sens. 105, 128–140.
Shi, X., Jiang, H., Zhang, L., Liao, M., 2017a. Landslide displacement monitoring with Split-bandwidth interferometry: a case study of the Shuping landslide in the three gorges area. Remote Sens. 9, 937.
Shi, X., Zhang, L., Tang, M., Li, M., Liao, M., 2017b. Investigating a reservoir bank slope displacement history with multi-frequency satellite SAR data. Landslides 14, 1961–1973.
Shi, X., Xu, Q., Zhang, L., Zhao, K., Dong, J., Jiang, H., Liao, M., 2019a. Surface displacements of the Heifangtai terrace in Northwest China measured by X and C-band InSAR observations. Eng. Geol. 259, 105181.
Shi, X., Yang, C., Zhang, L., Jiang, H., Liao, M., Zhang, L., Liu, X., 2019b. Mapping and characterizing displacements of active loess slopes along the upstream Yellow River with multi-temporal InSAR datasets. Sci. Total Environ. 674, 200–210.
Smith, A., Dixon, N., 2015. Quantification of landslide velocity from active waveguide–generated acoustic emission. Can. Geotech. J. 52, 413–425.
Tang, M., Xu, Q., Yang, H., Li, S., Iqbal, J., Fu, X., Huang, X., Cheng, W., 2019. Activity law and hydraulics mechanism of landslides with different sliding surface and permeability in the three gorges reservoir area, China. Eng. Geol. 260, 105212.
Terzaghi, K., Peck, R.B., Mesri, G., 1996. Soil Mechanics in Engineering Practice, 3rd ed. John Wiley & Sons, New York.
Ventura, G., Vilardo, G., Terranova, C., Sessa, E.B., 2011. Tracking and evolution of complex active landslides by multi-temporal airborne LiDAR data: the Montaguto landslide (southern Italy). Remote Sens. Environ. 115, 3237–3248.
Wang, F., Zhang, Y., Huo, Z., Peng, X., Wang, S., Yamasaki, S., 2008. Mechanism for the rapid motion of the Qianjiangping landslide during reactivation by the first impoundment of the three gorges dam reservoir, China. Landslides 5, 379–386.

Wang, J., 2011. Research on Formation Mechanism of Guobu Bank Slope in Front of Laxiwa Hydropower Station at Yellow River. Master Thesis. Chengdu University of Technology (In Chinese).
Xia, M., Ren, G.M., Li, T.B., Cai, M., Yang, T.J., Wan, Z.L., 2018. Complex rock slope deformation at Laxiwa Hydropower Station, China: background, characterization, and mechanism. Bull. Eng. Geol. Environ. 78, 3323–3336.
Xu, Q., Peng, D., Zhang, S., Zhu, X., He, C., Qi, X., Zhao, K., Xiu, D., Ju, N., 2020. Successful implementations of a real-time and intelligent early warning system for loess landslides on the Heifangtai terrace, China. Eng. Geol. 278, 105817.
Zhang, T., 2014. Engineering Geological Research on Large Deformation Characteristics of the Right Bank Slope in Front of One Power station's Dam on Yellow River Upstream. Master Thesis. Chengdu University of Technology (In Chinese).